Making Fiber-Shaped Ni//Bi Battery Simultaneously with High Energy Density, Power Density, and Safety

Mengying Wang, Songlin Xie, Chengqiang Tang, Yang Zhao, Meng Liao, Lei Ye, Bingjie Wang, and Huisheng Peng**

Fiber-shaped batteries are widely explored for a variety of important fields such as wearable electronics, information technology, internet of things, and public health. However, it remains difficult to simultaneously achieve high energy density, power density, and safety, which has largely limited their promising applications. Here, a new type of fiber-shaped Ni//Bi batteries with remarkable electrochemical performances is created from hierarchically 3D electrodes, where reduced graphene oxide sheets framed with Bi serve as the anode while reduced graphene oxide sheets wrapped with nickel oxide/nickel function as the cathode. The fiber-shaped Ni//Bi batteries show high energy density of 43.35 Wh kg^{-1} or 26.01 mWh cm^{-3} and high power density of 6600 W kg^{-1} or 3.96 W cm^{-3} with 96% capacity retention after 10 000 cycles. They are also safe with the use of aqueous electrolyte and can be further woven into the next-generation flexible textile-type power system. This work provides a general and efficient strategy to develop high-performance batteries by designing hierarchically structured electrodes.

1. Introduction

The rise of wearable electronics, information technology, internet of things, and public health has promoted the urgent development of fiber-shaped energy storage devices.[1–5] Energy density, power density, and safety are three key factors for the above applications of fiber-shaped energy storage devices.[6] For instance, the ever-increasing number and evolving type of wearable electronic devices that are integrated into an electronic fabric obviously require both high energy and power densities; they have been typically worn on human bodies, so they must be also safe enough during use. To date, two main categories of fiber-shaped energy storage devices are explored, i.e., supercapacitors[7–10] and batteries.[11–13] The fiber-shaped supercapacitors show high power density and high safety but with low energy density. The fiber-shaped batteries such as lithium-ion batteries generally demonstrate much higher energy density while both low power density and poor safety originated from the use of organic electrolytes that may be toxic and explode upon leakage. To the best of our knowledge, it remains challenging yet highly desiring to realize fiber-shaped energy storage devices that simultaneously display high energy density, power density, and safety.

Herein, a new type of fiber-shaped Ni//Bi batteries simultaneously with high energy density (43.35 Wh kg^{-1} or 26.01 mWh cm^{-3}), high power density (6600 W kg^{-1} or 3.96 W cm^{-3}), and high cycle life (96% capacity retention over 10 000 cycles) is designed from hierarchically 3D electrodes, where reduced graphene oxide (rGO) sheets framed with bismuth (Bi) serve as the anode while rGO sheets wrapped with nickel oxide (NiO)/Ni function as the cathode. The interlaced rGO/Bi/carbon nanotube (CNT) fiber anode was prepared by synchronically electroreduce and deposit GO and Bi^{3+} onto the CNT fiber due to their shared reduction potential (–1.2 V). The interlaced 3D structure contributed to a capacity increase from 51.26 to 146.9 mAh g^{-1}, in comparison to the bare Bi/CNT fiber electrode at 5 A g^{-1}. Partly thermal reduced rGO/Ni/NiO complex was introduced to form the hierarchical fiber cathode and contributed to a 115% capacity increase. The assembled fiber-shaped Ni//Bi battery exhibited a capacity of 163.7 mAh g^{-1} at 5 A g^{-1}, which also exhibited excellent tolerance against mechanical abuses even scissor cutting.

2. Results and Discussion

2.1. Morphology and Structure Characterization of the rGO/Bi/CNT Anode

The preparation of rGO/Bi/CNT anode is schematically illustrated in **Figure 1**a. Aligned CNT sheets were continuously drawn from CNT forests synthesized by chemical vapor deposition.[14] Several layers of CNT sheets could be stacked together along the drawing direction and twisted into a CNT fiber, which can be directly used as the backbone and current collector for Bi. Scanning electron microscopy (SEM) images of CNT fiber at different magnifications (Figure S1a–c, Supporting Information) revealed an aligned surface with high

---

M. Wang, S. Xie, C. Tang, Y. Zhao, M. Liao, L. Ye, Prof. B. Wang, Prof. H. Peng
Laboratory of Advanced Materials
State Key Laboratory of Molecular Engineering of Polymers
Department of Macromolecular Science
Fudan University
Shanghai 200438, China
E-mail: wangbingjie@fudan.edu.cn; penghs@fudan.edu.cn

The ORCID identification number(s) for the author(s) of this article can be found under https://doi.org/10.1002/adfm.201905971.

DOI: 10.1002/adfm.201905971

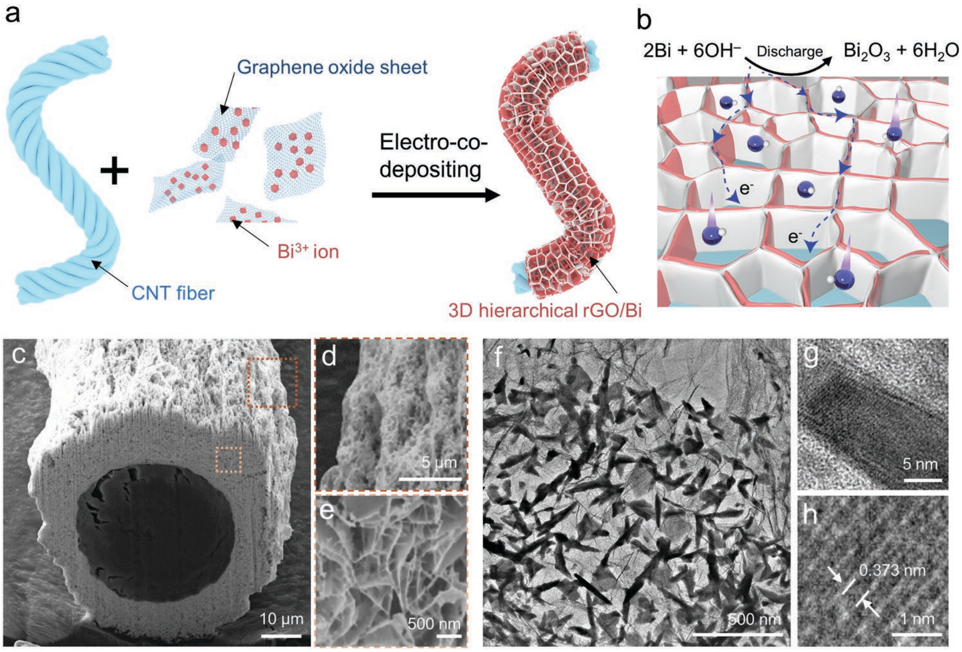

Figure 1. a) Schematic diagram of preparing the rGO/Bi/CNT anode. b) Electron transport and ion diffusion through the hierarchically 3D anode during discharging. c–e) Cross-sectional SEM images of rGO/Bi/CNT fiber with increasing magnifications. f) TEM image of rGO/Bi hybrid sheets with Bi deposited on the rGO sheet. g,h) High-resolution TEM images of the Bi at low and high magnifications, respectively.

roughness. The specific surface area of CNT fiber was determined to be 260.95 $m^2\ g^{-1}$ and the average diameter of pores was about 3 nm according to the N_2 adsorption–desorption profiles (Figure S1d,e, Supporting Information). Bi^{3+} and GO showed close reduction potential of appropriately −1.2 V, so they could be synchronically electrodeposited onto the CNT fiber. Moreover, this electro-co-deposition method contributed to an interlaced rGO/Bi 3D structure, which was beneficial for the ion diffusion and electron transport among the active materials (Figure 1b). To be specific, hydroxyl ions passed through the micropores during the discharge process and arrived at the active site, which successively caused the oxidation of bismuth and release of electrons. The resulting electrons transported through the 3D network formed by rGO, which helped them reach the CNT fiber rapidly.[15] SEM image clearly revealed the 3D interlaced rGO/Bi structure (Figure 1e), which produced a uniform distribution of C and Bi elements verified by energy dispersive spectroscopy (Figure S2, Supporting Information). 2D rGO layers guided the Bi metal to grow into the plane structure on or among rGO sheets and 1D fishbone-shaped rods across rGO edges.

Transmission electron microscopy (TEM) further displayed a uniform distribution of Bi nanocrystals on the rGO layer, where the diameter and length of bismuth were about 75–120 and 400–600 nm, respectively (Figure 1f). The nanosize of Bi crystals greatly benefits their efficient contact with rGO sheets. High-resolution TEM (Figure 1h) showed a lattice fringe spacing of 0.373 nm that matched well with the (101) plane spacing of the hexagonal phase of metallic Bi (Joint Committee on Powder Diffraction Standards #44-1246). X-ray diffraction (XRD) patterns (Figure S3, Supporting Information) further revealed a perfect agreement with standard crystalized bismuth (JCPDS #44-1246). All the distinct and isolated peaks of typical phases were found in the pattern, indicating a high crystallization of Bi, which was beneficial for the high electrochemical performance.[16] It should be noted that the diffraction peaks of C for graphene had not been observed from the XRD pattern of rGO/Bi hybrid. This may be explained by the high Bi deposition on rGO layers in the interlaced structure and dense stack of rGO sheets. Thermogravimetric analysis (TGA) of the rGO/Bi/CNT electrode was tested in air and only Bi_2O_3 was left in the container (Figure S4, Supporting Information). The mass ratio of Bi in the electrode was calculated to be 50.82%.

Raman spectra (Figure S5a, Supporting Information) of pristine Bi crystals and rGO/Bi hybrid displayed representative D and G bands of rGO at 1330 and 1560 cm^{-1}, respectively.[17] More importantly, the characteristic bands at 85.2 and 116.6 cm^{-1} for the hexagonal phase of Bi were observed, which was not only consistent with characteristic E_g and A_{1g} modes of metallic Bi,[18] but also in accordance with the high crystallization and purity indicated by the XRD characterization. X-ray photoelectron spectroscopy (XPS) of pristine Bi and rGO/Bi was further carried out to understand the cooperation effect of rGO and Bi. The survey spectrum mainly showed carbon, oxygen and bismuth elements in the materials (Figure S5b, Supporting Information). The peak located at 284.5 eV can be assigned to the characteristic peak of C1s, and the detailed analysis of C1s verified some residue oxygen-containing functional groups in rGO sheets, which was typically derived from the incomplete reduction based on electroreduction methods (Figure S5c, Supporting Information). Two fitted peaks in the XPS Bi 4f spectra with binding energies located at 157.7 and 163.0 eV represented the typical $4f_{7/2}$ and $4f_{5/2}$ peaks of Bi^0, respectively (Figure S5d, Supporting Information).[19] These results verified the interlaced and connected 3D structure for rGO sheets and highly crystallized bismuth.

2.2. The Electrochemical Properties of the rGO/Bi/CNT Anode

To examine the advantage of the 3D structured rGO/Bi/CNT hybrid, we prepared a control sample (named Bi/CNT) by directly electrodepositing Bi on the CNT fiber (Figure S6, Supporting Information), which was conducted in the deposition solution without GO. Bi nanoparticles were uniformly deposited on the CNT fiber, but the attachment of Bi nanoparticles was not stable enough as some were obviously peeled off from the CNT fiber (**Figure 2**b). Both above two fiber electrodes showed the same discharge plateaus at appropriately –0.53 and –0.38 V with the same charge plateau at appropriately –0.61 V (Figure 2c), revealing the same active material and reaction mechanism of the electrodes. However, the rGO/Bi/CNT fiber electrode delivered much higher specific capacity of 146.9 mAh g^{-1}, which was almost 2.5 times higher than that of the Bi/CNT fiber electrode. The rGO/Bi/CNT fiber electrode also showed higher capacity retention at high current density (Figure 2d and Figure S7, Supporting Information). At 25 A g^{-1}, the rGO/Bi/CNT fiber electrode showed capacity of 126.3 mAh g^{-1} which was about 73% retention of that at 1 A g^{-1}. In contrast, the specific capacity of the Bi/CNT fiber electrode dropped from 59.7 mAh g^{-1} at 1 A g^{-1} to 39.4 mAh g^{-1} at 25 A g^{-1} (Figure 2e and Figure S8, Supporting Information). The better electrochemical performance of the rGO/Bi/CNT fiber electrode may be ascribed to the designed 3D conducting network of the rGO/Bi hybrid, which in turn verified the expected high electron transport and ion diffusion among the active materials. The

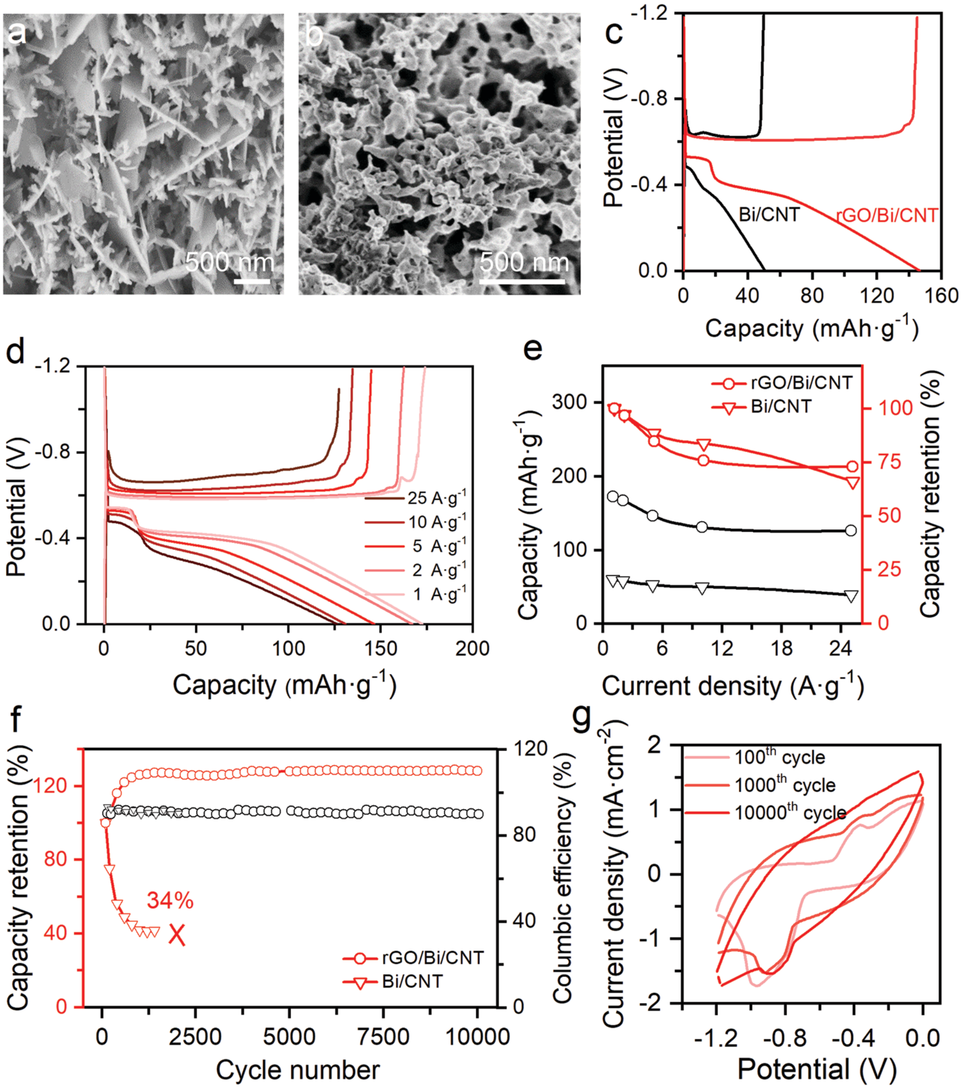

Figure 2. a,b) SEM images of rGO/Bi/CNT and Bi/CNT fibers, respectively. c) Charge and discharge profiles of rGO/Bi/CNT and Bi/CNT fiber electrodes at 5 A g^{-1}. d) Galvanostatic charge and discharge profiles of the rGO/Bi/CNT fiber electrode. e) Specific capacity and capacity retention of Bi/CNT and rGO/Bi/CNT fiber electrodes as a function of current density obtained from the galvanostatic charge/discharge curves. f) Cycling performance of rGO/Bi/CNT and Bi/CNT fiber electrodes at 100 mV s^{-1} for 2000 and 10 000 cycles. g) CV curves of the rGO/Bi/CNT fiber electrode at the 100th, 1000th, and 10 000th cycles.

relatively poor attachment between Bi nanoparticles and CNT fiber may result in slow electron transport and low material utilization.

As for the long-term stability, the capacity of the Bi/CNT fiber electrode decreased continuously during cycling at 100 mV s^{-1}, and only 34% of its initial capacity was maintained after 2000 cycles (Figure 2f). In contrast, the capacity of the rGO/Bi/CNT fiber electrode was initially increased and then well-maintained during 10 000 cycles at 100 mV s^{-1}. Note that the initial capacity increase was produced by the activation of the active materials. Figure S9 (Supporting Information) revealed that most active materials of the Bi/CNT fiber electrode had been peeled off from the CNT fiber after cycling, indicating the serious electrode pulverization during the charge/discharge process. However, the structure of rGO/Bi/CNT fiber was well preserved without exfoliation of GO sheets or cracks/fractures (Figure S10, Supporting Information).

To gain insights into the remarkable electrochemical properties of the rGO/Bi/CNT fiber, kinetics analysis was carried out via CV measurements (**Figure 3**a). Generally, energy storage by Faradaic processes occurs both on the surface (adsorption-controlled process) and in the bulk of the material (diffusion-controlled process). According to the relationship equation between the current and sweep rate of $j = \upsilon b$, the value of b can be calculated from the slope of a log(v)–log(j) plot.[20] Theoretically, for a b value of 0.5, the related electrochemical process is a diffusion-controlled process, whereas the value of 1.0 corresponds to an adsorption-controlled behavior.[21] The b value for the redox peak of rGO/Bi/CNT fiber electrode was 0.44 (Figure 3b), reflecting that the diffusion-controlled process provided the dominant capacity contribution. Therefore, the 3D hierarchical structure, which is beneficial for electron transport and ion diffusion, contributed to the good rate capability of the rGO/Bi/CNT fiber electrode.

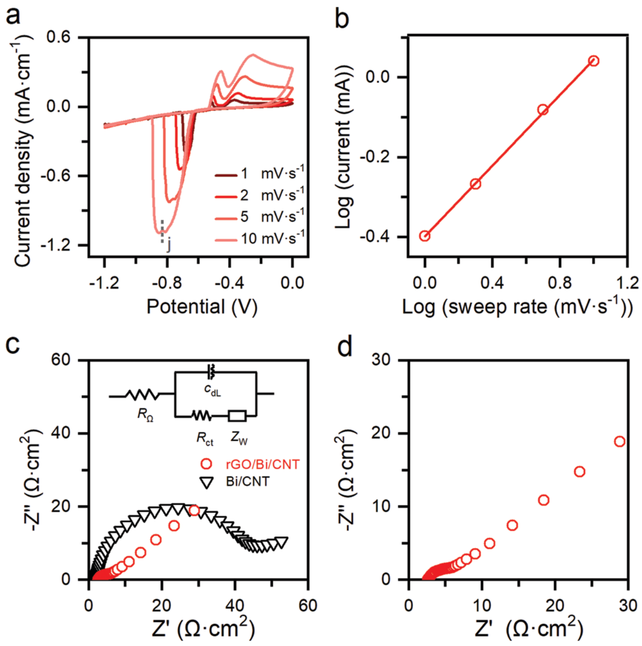

Figure 3. a) CV curves of the rGO/Bi/CNT fiber electrode at increasing scan rates. b) Determination of the b value according to the relationship between sweep rate and current of the rGO/Bi/CNT fiber electrode. c) EIS curves of the rGO/Bi/CNT and Bi/CNT fiber electrodes (inset, a simple equivalent circuit of the electrode). d) EIS curve of the rGO/Bi/CNT fiber electrode.

The high rate performance had been further confirmed by electrochemical impedance spectroscopy (EIS) tests, conducted at open circuit potential. Figure 3c presented the typical Nyquist plots of the rGO/Bi/CNT and Bi/CNT electrodes, both showing a straight line in the low-frequency region and a semicircle in the high-frequency region. A simple equivalent circuit (inset in Figure 3c), consisting of the bulk solution resistance ($R_Ω$), the charge transfer resistance (R_{ct}), the resistance related to the ion diffusion (R_w) and the double-layer capacitance (C_{dL}), was built to fit the EIS data. The $R_Ω$ of the two electrodes was almost the same (2.07 Ω for Bi/CNT and 2.63 Ω for rGO/Bi/CNT fiber electrode) because of the same testing environment. However, the R_{ct} of rGO/Bi/CNT fiber (3.52 Ω) was much smaller than that of Bi/CNT fiber (40.85 Ω), indicating greatly improved electrical conductivity of the active material. Moreover, the slope of the straight line in the low-frequency region for rGO/Bi/CNT fiber electrode is much steeper than that of Bi/CNT fiber electrode, showing a faster ion diffusion of the rGO/Bi/CNT electrode.

2.3. Morphology and Structure Characterization of the rGO/Ni/NiO Cathode

The hierarchical construction strategy was further verified in the Ni-based cathode design. Typically, rGO/Ni/NiO hybrids were deposited onto stacked CNT sheets and further twisted into the fiber with CNTs surrounded as the electron transport pathways. Nickel-based materials were synthesized by two steps. At the first step, NiO particles were uniformly grown on the rGO sheets by a solution phase reaction to form rGO/NiO hybrids. RGO was introduced for the following two reasons: i) the 2D rGO sheets can wrap the active materials inside under folding; ii) the 2D structure of rGO also ensures better contact with CNT fiber when the final active materials were wrapped into CNT sheets. At the second step, the rGO/NiO hybrids were annealed at 600 °C at Ar atmosphere for further reduction of both NiO and rGO to obtain rGO/Ni/NiO hybrids. The TGA of the rGO/Ni/NiO/CNT electrode was tested in air and only NiO was left in the container (Figure S11, Supporting Information). The mass ratio of Ni element in the electrode was calculated to be 59.00%. The introduction of the rGO sheets and Ni aimed at increasing the electrical conductivity of the active materials. It is worth mentioning that the average size of active materials was maintained at 30–70 nm before and after annealing (Figure S12, Supporting Information, and **Figure 4**a). It indicated that the calcination did not induce significant agglomeration which may benefit from the restriction of rGO layers. SEM images of rGO/Ni/NiO hybrids showed that Ni-based nanoparticles were uniformly distributed (Figure 4a), which can be further confirmed by the even distribution of C and Ni elements from the EDS (Figure S13, Supporting Information).

The crystal Ni/NiO nanoparticles on the rGO sheets ranged from 3 to 5 nm in size (Figure 4b), and they may aggregate into larger nanoparticles shown in Figure 4a. The lattice spacings

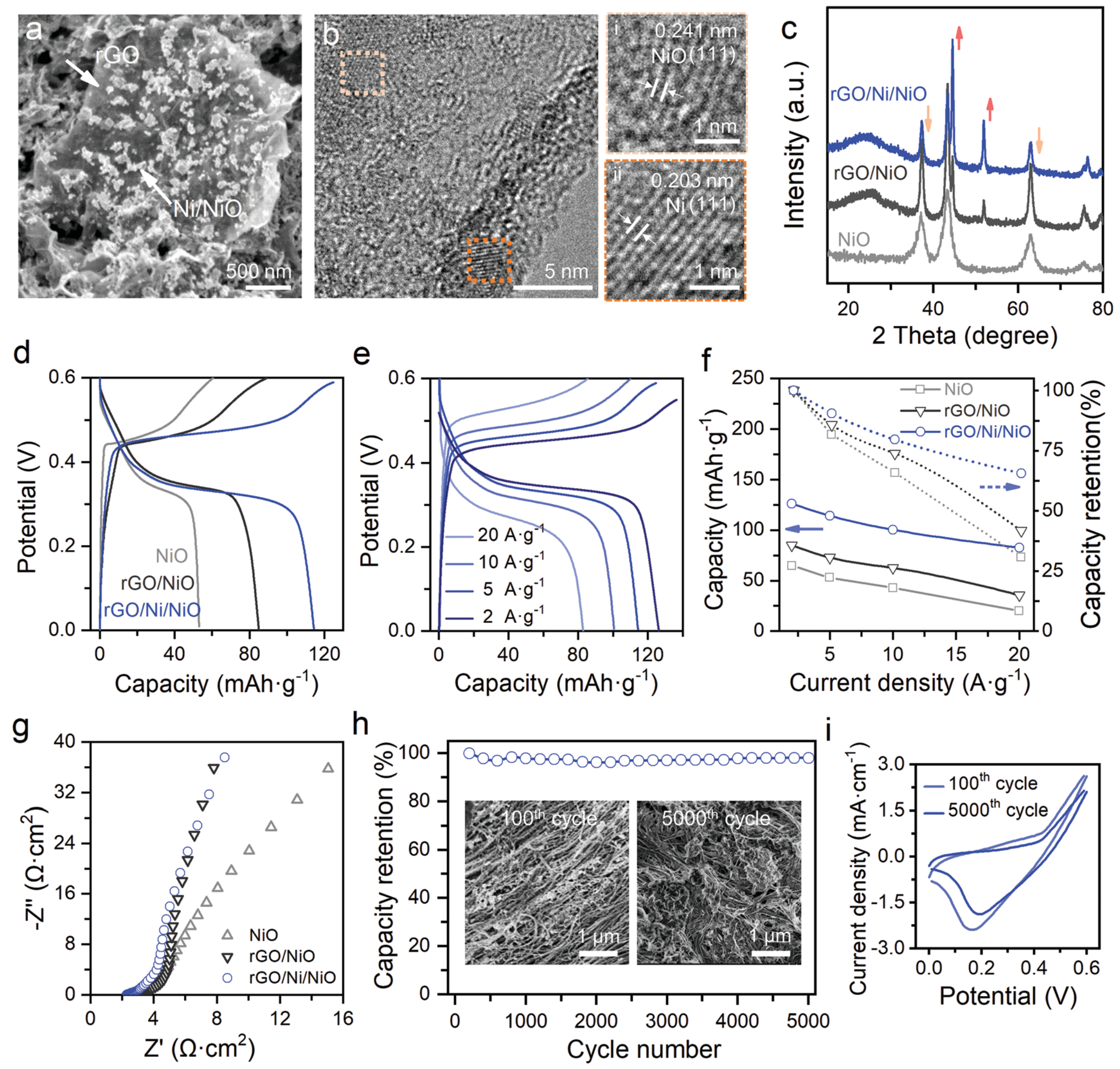

Figure 4. a,b) SEM and high-resolution TEM images of rGO/Ni/NiO hybrid, respectively. c) XRD patterns of NiO, rGO/NiO hybrid, and rGO/Ni/NiO hybrid. d) Charge and discharge profiles for NiO, rGO/NiO, and rGO/Ni/NiO fiber electrodes at current density of 5 A g^{-1}. e) Galvanostatic charge and discharge profiles of the rGO/Ni/NiO fiber electrode. f) Specific capacity and capacity retention of the NiO, rGO/NiO, and rGO/Ni/NiO fiber electrodes as a function of current density obtained from the galvanostatic charge/discharge curves. g) EIS curves of different fiber electrodes. h) Cycling performance of the rGO/Ni/NiO fiber electrode at 100 mV s^{-1} for 5000 cycles (inset, SEM images of the rGO/Ni/NiO fiber electrode after 100 and 5000 cycles). i) CV curves of the rGO/Ni/NiO electrode at the 100th and 5000th cycles.

of 0.241 and 0.203 nm corresponded to the (111) plane of the cubic phase of NiO and the (111) plane of the cubic phase of Ni, respectively. Typical XRD patterns of the rGO/Ni/NiO hybrid revealed a perfect agreement with the cubic NiO and Ni metal (JCPDS #47-1049 and #04-0850, respectively) (Figure 4c). Indeed, distinctive peaks of metallic Ni had already been observed in the XRD pattern of rGO/NiO, indicating the hydrazine hydrate might contribute to the reduction of NiO along with the reduction of GO.[22] The ratio of intensity of characteristic peaks of Ni to that of NiO in rGO/Ni/NiO hybrids was higher than that in rGO/NiO hybrid, which revealed the successful reduction of NiO to Ni in the annealing process. Therefore, NiO was partly reduced and wrapped by rGO sheets, which was further incorporated into the CNT sheets for both high electron transport and electrochemical performance.

2.4. The Electrochemical Properties of the rGO/Ni/NiO Cathode

CV tests were also made to clarify the capacitive behavior of the electrode material in 1 M KOH by a three-electrode system. Figure S14 (Supporting Information) showed the typical CV curves of the rGO/Ni/NiO/CNT hybrid electrode at increasing scan rates. All CV curves consisted of a pair of strong redox peaks, indicating that the capacitance characteristics were mainly governed by Faradaic redox reactions.[23] The cathodic peak occurred at around 0.15 V (vs Hg/HgO) indicated the reduction of NiOOH to $Ni(OH)_2$. The shapes of these CV curves showed almost no significant changes as the scan rates increased from 20 to 100 mV s^{-1}, implying both high electron transport and ion diffusion. With increasing scan rates, the potential of the oxidation peak shifted in the positive direction, while the potential of the reduction peak shifted in the negative direction, which was mainly related to the internal resistance of the electrode.[24]

Poor specific capacity and rate performance of NiO electrodes are usually caused by their poor electrical conductivity. Here, in order to demonstrate the advantage of the 3D conducting network formed by the rGO and Ni, galvanostatic charge/discharge tests of NiO, rGO/NiO and rGO/Ni/NiO/CNT fiber electrodes were conducted in 1 M KOH solution. Based on the prolongation of charge or discharge plateaus from charge–discharge curves (Figure 4d), the rGO/Ni/NiO/CNT fiber showed much higher specific capacity of 114.5 mAh g^{-1} at 5 A g^{-1}, compared to the NiO and rGO/NiO/CNT fiber. Moreover, the rGO/Ni/NiO/CNT fiber exhibited high capacity retention of 65.5% as the current density increased from 2 to 20 A g^{-1} (Figure 4e), while the corresponding capacity retention of NiO and rGO/NiO were only 30.8% and 41.8%, respectively (Figure 4f). Impressively, the rGO/Ni/NiO/CNT fiber showed lower polarization as the current density increased from 2 to 20 A g^{-1}, with the smallest voltage gap between discharge and charge platform increase of only ≈0.1 V, much lower than those of NiO/CNT and rGO/NiO/CNT fibers (0.15 V) (Figure S15, Supporting Information). The Coulombic efficiency of rGO/Ni/NiO/CNT fiber was also much higher than those of the control samples.

To better elucidate the enhanced electrochemical properties of the rGO/Ni/NiO/CNT fiber, EIS was conducted at open circuit potential (Figure 4g). The Ohmic resistance (R_s) is the sum of the electrolyte resistance, the intrinsic resistance of the active electrode materials and the contact resistance at the interface of the active materials and the current collector.[25] The smaller R_s of the rGO/Ni/NiO/CNT electrode (2.50 Ω cm^2) compared to rGO/NiO/CNT (3.01 Ω cm^2) fibers ensured better electrochemical performances. Moreover, the slopes of the straight line for rGO/NiO and rGO/Ni/NiO fibers were substantially steeper than that of NiO electrode, showing that the introduction of rGO offered faster ion diffusion rate. The electrode also showed excellent cycle stability (Figure 4h,i). After cycling, SEM images presented that the structure of the rGO/Ni/NiO/CNT fiber was well preserved, verifying the good cyclic stability of the electrode (Figure 4h, inset).

2.5. Electrochemical Properties of Fiber-Shaped Ni//Bi Full Battery

Finally, a fiber-based Ni//Bi full battery was fabricated by pairing rGO/Bi/CNT anode with rGO/Ni/NiO/CNT cathode in 1 M KOH (**Figure 5**a). Based on the different potential ranges of the two electrodes, the stable operating voltage of this Ni-Bi battery was extended to 1.8 V without decomposition of the aqueous electrolyte (Figure 5b). According to the galvanostatic charge and discharge profiles (Figure 5c), the capacities of rGO/Ni/NiO cathode and rGO/Bi anode were well matched when the operation window was 1.8 V. Figure 5d showed the typical galvanostatic charging/discharging curves of the fiber-shaped Ni//Bi battery at increasing current densities. It exhibited a high specific capacity of 163.7 mAh g^{-1} at 5 A g^{-1} with a stable charging platform, indicating the efficient redox reaction. The Coulombic efficiency of the battery was stable and close to 100%, revealing its good reversibility. When the current density increased to 25 A g^{-1}, a high capacity of 98.2 mAh g^{-1} (about 60% of the initial capacity) was maintained with a short charge/discharge time of only 15 s, manifesting its extraordinary rate performance.

The unsatisfactory of cycling performance is one of the major bottlenecks for fiber-shaped batteries. The long-term stability of fiber-shaped Ni//Bi battery was examined between 0 and 1.8 V at a scan rate of 100 mV s^{-1} for 10 000 cycles. Figure 5e showed the capacitance retention of the Ni//Bi battery charged at 1.8 V as a function of cycle number. Significantly, it exhibited high cycling durability with 96.2% retention of the original capacity after 10 000 cycles, outperforming most previous fiber-based aqueous batteries, such as carbon networks @Fe_7S_8@Graphene//$Na_3V_2(PO_4)_3$@C battery (63.4% capacity retention after 50 cycles),[26] Zn//Co battery (71.1% capacity retention after 5000 cycles),[27] and MWCNT@LTO//MWCNT@LMO battery (85% capacity retention after 100 cycles).[28] The CV profiles displayed little capacity attenuation after 10 000 cycles (inset in Figure 5e), again clarifying the outstanding cycling stability of the fiber-shaped Ni//Bi battery. In order to further confirm its cycling performance, continuous charging/discharging test was also conducted. And it exhibited high cycling stability with 91.6% retention of the original capacity after 5000 cycles. Figure S16b (Supporting Information) displayed the stable galvanostatic charge and discharge profiles during cycling.

The energy and power densities are generally used as important parameters to characterize the electrochemical performance of the battery. It remains challenging to realize both high energy and power densities for fiber-shaped aqueous batteries. Figure 5f compared the Ragone plots of fiber-shaped Ni//Bi battery with the previous fiber-based aqueous batteries and supercapacitors. A maximal energy density of 43.35 Wh kg^{-1} or 26.01 mWh cm^{-3} was gained by the fiber-shaped Ni//Bi battery, which was remarkably higher than that of fiber-based aqueous lithium-ion batteries[29] and thin-film lithium-ion batteries. Notably, a maximum power density of 6.6 kW kg^{-1} or 3.96 W cm^{-3} has been also achieved based on the weight or volume of the two fiber electrodes by the fiber-shaped Ni//Bi battery, which is around 25 times higher than that of the supercapacitor based on CNT@CMC[25] and 10 times higher than that of commercially available supercapacitors (3.5 V/25 mF and 5.5 V/100 mF). As compared to the hybrid fiber-shaped energy storage device[30] that integrated battery and supercapacitor together, the fiber-shaped Ni//Bi battery possessed five times higher energy density and higher power density.

The 1D configuration rendered the Ni//Bi battery with high flexibility (Figure S17, Supporting Information). The fiber-shaped Ni//Bi battery was bent to 45°, 90°, 135°, and 180° without obvious damages in structure, and the capacity was well-maintained under different bending conditions (Figure S18a, Supporting Information). Figure S18b (Supporting Information) further compared the discharge performance before and after bending (bending to 90° for 1000 times), and only 8.7% capacity was lost after 1000 cycles of bending. For wearable applications, the fiber-shaped

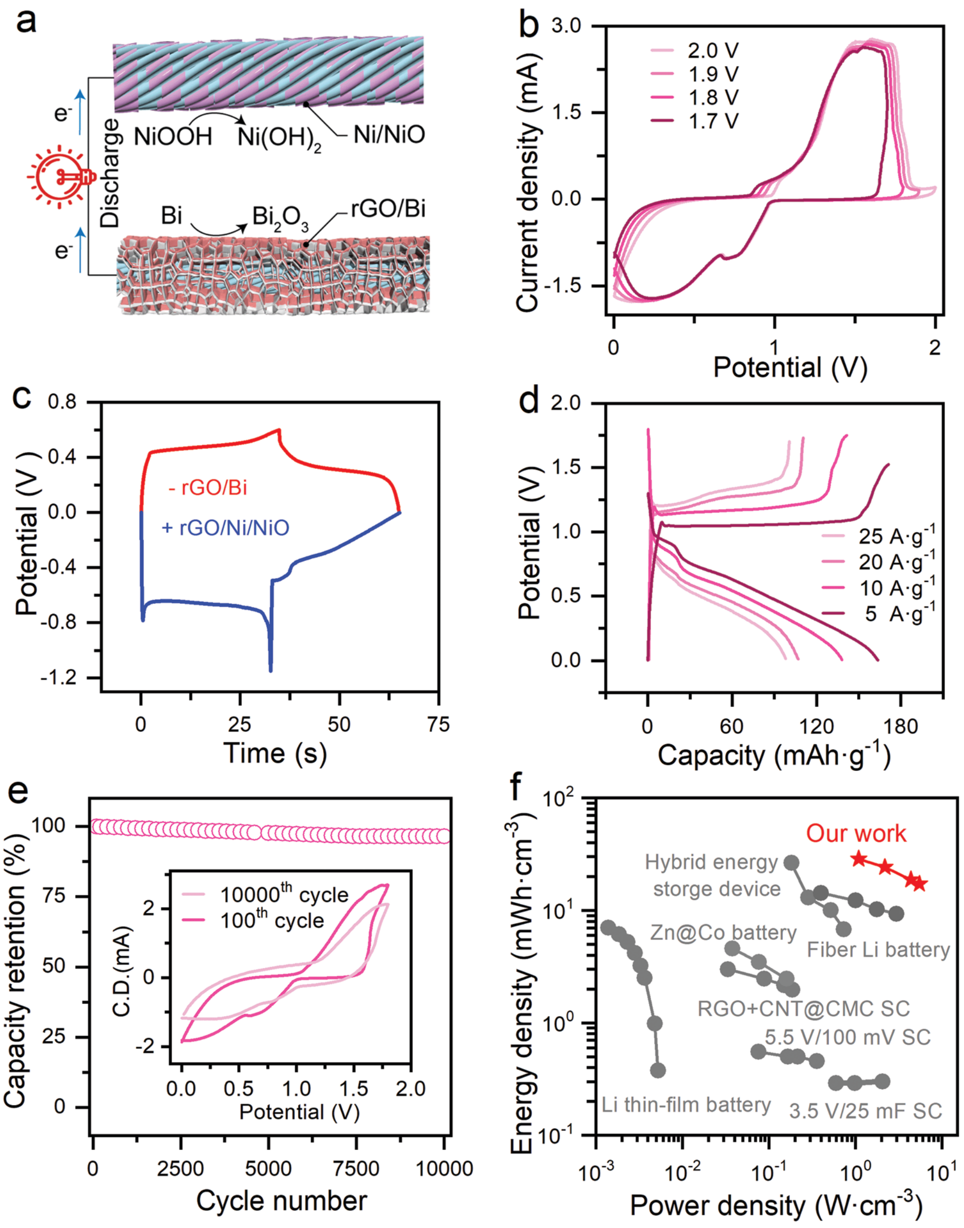

Figure 5. a) Schematic diagram of the working mechanism of the fiber-shaped Ni//Bi full battery. b) CV curves with different operating voltage windows at 100 mV s^{-1}. c) Galvanostatic charge and discharge profiles of the rGO/Bi/CNT and rGO/Ni/NiO/CNT fiber electrodes at current density of 0.6 mA cm^{-1}. d) Galvanostatic charge and discharge profiles. e) Cycling performance at 100 mV s^{-1} for 10 000 cycles (inset, CV curves at the 100th and 10 000th cycles). f) Ragone plots by comparing the fiber-shaped Ni//Bi full battery with the other energy storage devices.

batteries can be directly woven into flexible power textiles, or the active material can be deposited on the conducting fiber textile. To demonstrate the high safety of the fiber-shaped Ni//Bi battery, three energy fabrics were connected in series to power an electronic watch (3 V) (Figure S19a, Supporting Information). More importantly, when a scissor was used to cut the fabrics (Figure S19b, Supporting Information), the textile batteries were effectively operated. No obvious electrolyte leakage was found and the electronic watch worked well. The battery textile efficiently powered the electronic watch even after being cut into half (Figure S19c, Supporting Information).

3. Conclusion

To summarize, we have designed a new family of fiber-shaped Ni//Bi batteries with high energy density, high power density, and high safety through the hierarchically 3D design of the electrode. They provide an efficient solution to the key problem on the development of fiber-shaped energy storage devices that simultaneously require high energy, power, and safety during practical applications. This work may also open a new avenue to make high-performance batteries, particularly flexible power systems, by optimizing the structure of hybrid electrode materials.

4. Experimental Section

Preparation of the rGO/Bi/CNT Hybrid Fiber: GO solution was synthesized via a modified Hummer's method.[31] Aligned CNT arrays were synthesized by typical chemical vapor deposition. CNT sheets with a thickness of about 18 nm were drawn out of the arrays with a width of about 2 cm. Eight CNT sheets stacked along the drawing direction were strolled into a fiber. The rGO/Bi composite was synthesized on the CNT fiber by electrodeposition at room temperature using a CHI760 electrochemical workstation. The electrodeposition was conducted in a solution (40 mL) containing graphene oxide (0.03 mg mL^{-1}), ethylenediaminetetraacetic acid disodium salt (EDTA·2Na, 0.1 M) and $Bi(NO_3)_3 \cdot 5H_2O$ (50 × 10^{-3} M). Carbon rod and Hg/HgO electrode were used as counter and reference electrodes, respectively. A potential of −1.2 V versus Hg/HgO electrode was applied for 60 s. After electrodeposition, the sample was washed with water and dried at 80 °C in air. The mass of the rGO/Bi composite loaded on the electrode (50.0 ± 1.0 µg cm^{-1}) was measured by a microbalance (Sartarious SE2, resolution of 0.1 µg). Finally, the sample was dipped in graphene oxide solution (1.5 mg mL^{-1}) for ten times and dried at 80 °C in air.

Preparation of the Bi/CNT Hybrid Fiber: As a comparison, the Bi/CNT hybrid fiber was synthesized on the CNT fiber by electrodeposition at room temperature using a CHI760 electrochemical workstation. The electrodeposition was conducted in a solution (40 mL) containing EDTA·2Na (0.1 M), $Bi(NO_3)_3 \cdot 5H_2O$ (50 × 10^{-3} M) and hexadecyl trimethyl ammonium bromide (10 × 10^{-3} M). Carbon rod and Hg/HgO electrode were used as counter and reference electrodes, respectively. Bi was deposited on the CNT fiber by applying −0.9 V for 30 min. The sample was washed with deionized water, dried at 80 °C in air and then measured to decide the mass with the balance. Then, the sample was dipped in graphene oxide solution (1.5 mg mL^{-1}) for ten times and dried at 80 °C in air. The weights of the yarns were measured by a microbalance (Sartarious SE2, resolution of 0.1 µg).

Preparation of the rGO/Ni/NiO Hybrid: GO was synthesized via a modified Hummer's method. NiO nanoparticles were synthesized by wet chemical sol–gel method.[32] The as-prepared GO (1 mg mL^{-1}) and NiO nanoparticles (3 mg mL^{-1}) were uniformly dispersed in deionized water by ultrasonication at 60 °C for 30 min. Subsequently, hydrazine hydrate (95%) solution was added to the resultant mixture (1:200) to reduce the GO and kept continuous stirring at 60 °C for 12 h. The mixture was then centrifuged, and the obtained precipitate was washed several times with deionized water and ethanol, followed by vacuum drying for overnight at 60 °C to obtain rGO/NiO hybrid. Finally, rGO/Ni/NiO hybrid was obtained by annealing rGO/NiO hybrid in argon at 600 °C for 2 h.

Preparation of the rGO/Ni/NiO/CNT Hybrid Fiber: The rGO/Ni/NiO hybrid (12 mg) was dispersed in ethanol (2 mL) by ultrasonication at 60 °C for 10 min. Then eight stacked CNT sheets drawn from a spinnable CNT array were immersed in the suspension and later scrolled into an rGO/Ni/NiO/CNT hybrid fiber. The mass of the rGO/Ni/NiO hybrid loaded on the electrode (63.5 ± 0.5 µg cm^{-1}) was measured by a microbalance (Sartarious SE2, resolution of 0.1 µg).

Assembly of the Fiber-Shaped Ni//Bi Battery: The Ni//Bi full battery was assembled by pairing the rGO/Bi/CNT hybrid electrode (1 × 2 cm) and the rGO/Ni/NiO/CNT electrode (1 × 2 cm) in 1 M KOH aqueous solution.

Material Characterization: SEM images were captured on a scanning electron microscopy (Carl Zeiss Ultra 55) performed at an acceleration voltage of 5 kV. EDS mappings were acquired from a scanning electron microscopy (Carl Zeiss Ultra 55) at 15 kV. TEM images were obtained from a transmission electron microscopy (FEI Tecnai G2 20 TWIN) performed at an acceleration voltage of 200 kV. Raman spectra were acquired on a confocal Raman microscope (HORIBA XploRA) using a 50 × objective and 532 nm laser. The structures of materials were further characterized by XPS (ESCALab250, Thermo VG) and XRD (D8 ADVANCE). TGA (PerkinElmer instruments Pyris) was conducted in air from 50 to 800 °C at a heating rate of 10 °C min^{-1}.

Electrochemical Measurement: CV, galvanostatic charge/discharge measurements, and electrochemical impedance spectroscopy were conducted using an electrochemical workstation (CHI 660D). The electrochemical studies were carried out in a three-electrode system. The hybrid fiber directly served as the working electrode without any binders or conductive additives. A carbon rod was used as the counter electrode with Hg/HgO (in 1 M KOH) as the reference electrode (+0.1 V vs SHE at 25 °C). 1 M KOH aqueous solution was used as the electrolyte. EIS was conducted from 100 mHz to 100 kHz at a voltage amplitude of 10 mV. All electrochemical measurements of the Ni//Bi full battery were performed in 1 M KOH aqueous solution. The mass specific capacities (C_m) were calculated from the charge and discharge profiles according to $C_m = (I\Delta t)/m$, where I, Δt, and m correspond to the applied current (mA), discharge time (h), and the mass of the active material of the anode electrode (g), respectively. The mass specific capacity of the full battery was calculated from the mass of the active material of the anode. The calculations of the energy and power densities were based on the overall mass or volume of the anode and the cathode.

Supporting Information

Supporting Information is available from the Wiley Online Library or from the author.

Acknowledgements

M.W. and S.X. contributed equally to this work. This work was supported by MOST (2016YFA0203302), NSFC (21634003, 51573027, 51673043, 21604012, 21805044, and 21875042), STCSM (16JC1400702, 17QA1400400, 18QA1400700, and 18QA1400800), SHMEC (2017-01-07-00-07-E00062), and Yanchang Petroleum Group. Part of the sample fabrication was performed at Fudan Nano-fabrication Laboratory.

Conflict of Interest

The authors declare no conflict of interest.

Keywords

aqueous batteries, fiber-shaped, hierarchically 3D

Received: July 23, 2019
Revised: September 22, 2019

---

[1] A. K. Yetisen, J. L. Martinez-Hurtado, B. Ünal, A. Khademhosseini, H. Butt, *Adv. Mater.* **2018**, *30*, 1706910.
[2] X. Xu, S. Xie, Y. Zhang, H. Peng, *Angew. Chem., Int. Ed.* **2019**, *58*, 13643.
[3] W. Shi, Y. Guo, Y. Liu, *Adv. Mater.* **2019**, 1901493.
[4] L. Kou, T. Huang, B. Zheng, Y. Han, X. Zhao, K. Gopalsamy, H. Sun, C. Gao, *Nat. Commun.* **2014**, *5*, 3754.
[5] X. Xu, S. Li, J. Chen, S. Cai, Z. Long, X. Fang, *Adv. Funct. Mater.* **2018**, *28*, 1802029.
[6] W. Tauze, *Nature* **2015**, *526*, S105.
[7] J. Bae, M. K. Song, Y. J. Park, J. M. Kim, M. Liu, Z. L. Wang, *Angew. Chem., Int. Ed.* **2011**, *50*, 1683.
[8] G. Qu, J. Cheng, X. Li, D. Yuan, P. Chen, X. Chen, B. Wang, H. Peng, *Adv. Mater.* **2016**, *28*, 3646.
[9] X. Li, X. Zang, Z. Li, X. Li, P. Li, P. Sun, X. Lee, R. Zhang, Z. Huang, K. Wang, D. Wu, F. Kang, H. Zhu, *Adv. Funct. Mater.* **2013**, *23*, 4862.

[10] B. Wang, X. Fang, H. Sun, S. He, J. Ren, Y. Zhang, H. Peng, *Adv. Mater.* **2015**, *27*, 7854.
[11] Y. Xu, Y. Zhang, Z. Guo, J. Ren, Y. Wang, H. Peng, *Angew. Chem.* **2015**, *127*, 15610.
[12] H. Lin, W. Weng, J. Ren, L. Qiu, Z. Zhang, P. Chen, X. Chen, J. Deng, Y. Wang, H. Peng, *Adv. Mater.* **2014**, *26*, 1217.
[13] Y. Zeng, Y. Meng, Z. Lai, X. Zhang, M. Yu, P. Fang, M. Wu, Y. Tong, X. Lu, *Adv. Mater.* **2017**, *29*, 1702698.
[14] K. Jiang, Q. Li, S. Fan, *Nature* **2002**, *419*, 801.
[15] H. Sun, S. Xie, Y. Li, Y. Jiang, X. Sun, B. Wang, H. Peng, *Adv. Mater.* **2016**, *28*, 8431.
[16] P. Zhang, Y. Zeng, M. Wang, W. Xu, Y. Liu, X. Lu, *J. Mater. Chem. A* **2018**, *6*, 8895.
[17] G. K. Ramesha, S. Sampath, *J. Phys. Chem. C* **2009**, *113*, 7985.
[18] S. Onari, M. Miura, K. Matsuishi, *Appl. Surf. Sci.* **2002**, *197–198*, 615.
[19] C. Wang, C. Shao, L. Wang, L. Zhang, X. Li, Y. Liu, *J. Colloid Interface Sci.* **2009**, *333*, 242.
[20] V. Augustyn, J. Come, M. A. Lowe, J. W. Kim, P.-L. Taberna, S. H. Tolbert, H. D. Abruña, P. Simon, B. Dunn, *Nat. Mater.* **2013**, *12*, 518.
[21] P. Simon, Y. Gogotsi, B. Dunn, *Science* **2014**, *343*, 1210.
[22] A. Pandey, R. Manivannan, *Int. J. Eng. Res. Appl.* **2015**, *5*, 96.
[23] J. Liu, M. Chen, L. Zhang, J. Jiang, J. Yan, Y. Huang, J. Lin, H. J. Fan, Z. X. Shen, *Nano Lett.* **2014**, *14*, 7180.
[24] Y. Zeng, Z. Lin, Y. Meng, Y. Wang, M. Yu, X. Lu, Y. Tong, *Adv. Mater.* **2016**, *28*, 9188.
[25] N. Ogihara, Y. Itou, T. Sasaki, Y. Takeuchi, *J. Phys. Chem. C* **2015**, *119*, 4612.
[26] W. Chen, X. Zhang, L. Mi, C. Liu, J. Zhang, S. Cui, X. Feng, Y. Cao, C. Shen, *Adv. Mater.* **2019**, *31*, 1806664.
[27] M. Li, J. Meng, Q. Li, M. Huang, X. Liu, K. A. Owusu, Z. Liu, L. Mai, *Adv. Funct. Mater.* **2018**, *28*, 1802016.
[28] J. Ren, Y. Zhang, W. Bai, X. Chen, Z. Zhang, X. Fang, W. Weng, Y. Wang, H. Peng, *Angew. Chem., Int. Ed.* **2014**, *53*, 7864.
[29] Y. Zhang, Y. Wang, L. Wang, C.-M. Lo, Y. Zhao, Y. Jiao, G. Zheng, H. Peng, *J. Mater. Chem. A* **2016**, *4*, 9002.
[30] Y. Zhang, Y. Zhao, X. Cheng, W. Weng, J. Ren, X. Fang, Y. Jiang, P. Chen, Z. Zhang, Y. Wang, *Angew. Chem., Int. Ed.* **2015**, *54*, 11177.
[31] D. Li, M. B. Müller, S. Gilje, R. B. Kaner, G. G. Wallace, *Nat. Nanotechnol.* **2008**, *3*, 101.
[32] A. Roychoudhury, S. Basu, S. K. Jha, *Biosens. Bioelectron.* **2016**, *84*, 72.